Particle Accelerators, 1971, Vol. 2, pp. 149–167

HELICAL WAVEGUIDES FOR HEAVY PARTICLE LINACS†

A. J. SIERK, C. J. HAMER, AND T. A. TOMBRELLO
California Institute of Technology, Pasadena, California, U.S.A.

The properties of helical waveguides for use as heavy particle accelerators are investigated, and a new method of focusing is proposed that involves neither quadrupoles nor shaped electrodes. These calculations include estimates of mechanical stability, electrical losses, and the effects of finite helix wire size. In addition, the double helix waveguide is analyzed; this structure may be practical for ions with initial velocities below 0.01 C.

1. INTRODUCTION

Early in the history of linear accelerators, it was suggested that helical transmission lines might provide a practical method of achieving a low velocity traveling wave for accelerating heavy particles.[1–3] During the period 1950–1958, several theoretical analyses were made,[3,4] indicating that the structure could be competitive with an Alvarez[5] linac. Several groups constructed various models,[6–10] and one group built a small working accelerator.[10] This work was not pursued, as there appeared to be only marginal differences in efficiency between the two designs, and problems of breakdown in the dielectric supports of the helix were encountered. The Alvarez design was perfected by this time and performed satisfactorily. In the following decade, a group at Frankfurt continued work on the helical structure,[11] and has constructed a small accelerator.[12]

There are several reasons for considering a helical transmission line for use as a particle accelerator. This structure can have phase velocities from 0.01 C to nearly C. When the helix is operated as a standing-wave resonator, one may achieve a low frequency which is nearly independent of transverse dimensions. The field distribution is quite homogeneous, so that large phase-space acceptance, simple alignment, and improved focusing properties can be obtained.

In this paper, we present a brief review of previous treatments of the electromagnetic properties of the helical transmission line, followed by calculations of the effects of finite-wire helix coils, and distortions and frequency shifts caused by gravity and by electromagnetic forces. An improved focusing method, well suited to helical linacs, but also useful for other configurations is explained. Finally, the double helix, which offers significant advantages in accelerators is analyzed. Because this study was undertaken with the thought of designing a superconducting accelerator, a brief mention is made of properties of superconductors. Most of the results presented do not depend on the use of superconducting materials; however, our bias in that direction is reflected in some of the choices of parameters given in the figures.

The units used in all formulae and graphs are Gaussian cgs, unless explicitly stated to be otherwise, for example in relating E_0 to energy gain.

2. SUPERCONDUCTING ACCELERATORS

An important limitation upon the energy gain of present linear accelerators is the rf power expended in ohmic losses in the resonating structure. The magnitude of these losses usually requires that the power introduced be pulsed, often with duty factors limited to less than 1 per cent. This pulsing restricts the average beam current, and in practice limits the energy resolution of the final beam.

Constructing an accelerator from superconductors, whose surface resistance is lower by 10^{-5} to 10^{-7} may make possible continuous duty cycle operation at higher field gradients than are now employed. The rf power source for such a device would be significantly smaller, since the only power needed would be to accelerate the beam, with losses a negligible factor.

An article by Schwettman *et al.*,[13] considers in detail many factors of importance for superconducting accelerator design. A few of these are mentioned here:

In order to remain in the superconducting state, the material must operate below its transition temperature, a few °K for usable materials. This means the structure must be kept near the temperature of liquid helium. Theoretical calculations[13] verified by experiments,[14] show that

† Supported in part by the National Science Foundation (GP-15286, GP-9114, GP-19887) and the Office of Naval Research (Nonr-220(47)).

the surface resistance of niobium varies nearly as $(\omega^2/T)\exp(-\epsilon_g/2k_BT)$, for the range 1–4 °K. This implies one would desire even lower temperatures, but with obvious economic limitations. Because of the improved heat transport properties of liquid helium II, it will probably be desirable to operate below the λ point (2.2 °K).

Considerations of present refrigerator costs[13,15] put a practical upper limit on rf losses of 1–5 W/ft of structure. Since losses are proportional to $|B_{\|}|^2$ at the superconducting surface, one desires low B fields at all superconducting surfaces to minimize losses. This limitation is also imposed by the critical field transition in the superconductor. Above a certain applied magnetic field level, $H_c(T)$, the superconductor makes a transition to the normal state. This consideration singles out the elements lead and niobium as the only practical alternatives. Lead has a dc critical field ($T = 0$) of about 800 Oe., while in niobium, the thermodynamic critical field is nearly 1950 Oe.[16] However, at radio frequencies, the transition always occurs at lower apparent field levels. Experiments on niobium cavities have achieved a critical field of about 1100 Oe at 8 GHz.[14] For lead structures, a value of 660 Oe at 750 MHz has been reported.[17] It must be emphasized that practical operating levels may be appreciably lower than these figures.

There is a limitation on electric fields imposed by electron field emission. The actual limiting value is a strong function of microscopic surface smoothness, and depends greatly on how the sample is prepared. Workers at Stanford have achieved levels of 70 MV/m without breakdown in carefully annealed niobium cavities.[14] A group at Karlsruhe reports Q degradation due to field emission in lead-plated cavities at fields near 30 MV/m.[17] This phenomenon is nearly independent of temperature, so the same type of limitation applies to normal materials.

In complicated geometries like the helical waveguide, it may be desirable to include dielectric supports to provide mechanical stability. All dielectrics involve losses, and the energy lost in 1 cm³ of material per second in a standing wave is

$$\frac{\epsilon\nu\tan\delta\,|E|^2}{4},$$

where ϵ is the real dielectric constant, and δ is the loss angle. E is in Gaussian units, and ν in hertz. For $\tan\delta \sim 10^{-6}$ and a frequency of 10 MHz, this rate is about 0.3 W/cm³. This would limit dielectric material to about 10 cm³ per foot of structure, with proportionally less allowed at higher frequencies.

For a room-temperature machine, only the limitation on the electric field remains. One still wishes to minimize losses, but there is no limit on the B field, and the power lost in dielectrics would be much less than the resistive dissipation.

3. THE HELICAL TRANSMISSION LINE

The helical transmission line is formed of a wire coiled into a helical shape, surrounded by a coaxial, cylindrical conductor (see Fig. 1). For low

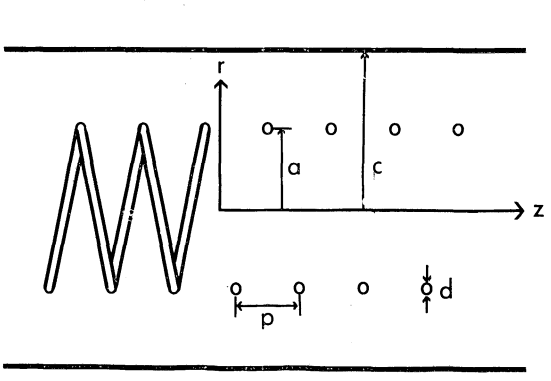

FIG. 1. Diagram of single helix geometry, defining a, c, d, p, and the r and z axes.

frequencies and small pitch angles the propagation velocity is given by $v \sim 1/(L_0 C_0)^{1/2}$ where L_0 is the inductance per unit length of the coil, and C_0 is the capacitance per unit length of a cylindrical capacitor of the dimensions of the coil and shield. For higher frequencies, $v \sim C\sin\theta$, corresponding to a signal propagating along the helix wire. A sinusoidal current propagates around the coil, setting up a wave consisting of a TM component, and an interlocked TE component. The TM component is the portion of interest for accelerators, as it has a large axial electric field.

A. *The Sheath Model*

The usual method of obtaining the field distribution in this structure makes use of the sheath model.[18,19] In this treatment, the coil is replaced by an infinitely thin sheath which conducts perfectly only in the direction of the coils. This model gives very accurate values for the phase velocity and fields (except in the neighborhood of the coils) for frequencies corresponding to wavelengths much longer than the pitch. The 'tape model'[20,21] is a

generalization of the sheath model which takes into account the periodicity of the helix by replacing the helix wires by flat tapes. The solution to the tape helix is constructed of a superposition of the basic sheath helix mode with additional higher order modes not having azimuthal symmetry.

The analysis using the sheath model has been given elsewhere,[11,19,20] so we will summarize this treatment only briefly here. In the cylindrical coordinates of the waveguide (see Fig. 1), the general field distribution is a sum over partial waves, each of the form (see Appendix A for definitions of symbols)

$$\text{TM:}\quad E_z^m(r,\phi,z,t) = E_z^m(r)\, e^{i\omega t}\, e^{im\phi}\, e^{-ib_m z} \tag{1}$$

$$\text{TE:}\quad B_z^m(r,\phi,z,t) = B_z^m(r)\, e^{i\omega t}\, e^{im\phi}\, e^{-ib_m z} \tag{2}$$

$E_z^m(r)$ and $B_z^m(r)$ are solutions to Bessel's equation[20,21]

$$\left[\frac{d^2}{dr^2}+\frac{1}{r}\frac{d}{dr}+\left(k^2-b_m^2-\frac{m^2}{r^2}\right)\right]\cdot\begin{bmatrix}E_z^m(r)\\ B_z^m(r)\end{bmatrix}=0. \tag{3}$$

The components E_r^m, E_ϕ^m, B_r^m, B_ϕ^m may be derived from E_z^m and B_z^m by the usual methods[22]

$$\begin{aligned}
E_r^m(r) &= \frac{ib_m}{g_m^2}\frac{\partial E_z^m(r)}{\partial r},\\
E_\phi^m(r) &= -\frac{mb_m}{g_m^2 r}E_z^m(r)-\frac{ik}{g_m^2}\frac{\partial B_z^m(r)}{\partial r},\\
B_r^m(r) &= \frac{ib_m}{g_m^2}\frac{\partial B_z^m(r)}{\partial r},\\
B_\phi^m(r) &= -\frac{mb_m}{g_m^2 r}B_z^m(r)+\frac{ik}{g_m^2}\frac{\partial E_z^m(r)}{\partial r}.
\end{aligned} \tag{4}$$

Since $b_m^2(=\omega^2/v^2) > k^2(=\omega^2/C^2)$, the wave being slower than C, Eq. (3) becomes a modified Bessel's equation with the solutions $I_m(g_m r)$, $K_m(g_m r)$ $(g_m^2 = b_m^2 - k^2)$. Because of the azimuthal symmetry of the sheath, only $m = 0$ components appear in the solution.

There are eight independent field amplitudes, or seven ratios, considering one amplitude arbitrary. Two are trivially eliminated by the condition that the coefficients of $K_0(g_0 r)$ must be zero inside the sheath, since K_0 becomes infinite at $r = 0$. There are two boundary conditions at $r = c$: $E_\parallel = 0$ and $B_\perp = 0$. There are four boundary conditions at $r = a$: E_z and E_ϕ are continuous across the sheath, the component of E along the conducting direction $(E_z \sin\theta + E_\phi \cos\theta)$ is zero and the component of B in this direction is continuous. Thus, there are six conditions on the five non-zero field amplitude ratios. The extra equation results in a dispersion relation

$$v = \frac{C\tan\theta}{\gamma}\left[\frac{I_0(g_0 a)I_1(g_0 c)}{I_0(g_0 c)I_1(g_0 a)}\cdot\left(\frac{K_0(g_0 a)I_0(g_0 c)-I_0(g_0 a)K_0(g_0 c)}{K_1(g_0 a)I_1(g_0 c)-I_1(g_0 a)K_1(g_0 c)}\right)\right]^{1/2}. \tag{5}$$

The boundary conditions at the sheath which mix the ϕ and z components cause a mixing of the TM and TE modes in any propagating wave. Figure 2 shows this dispersion equation plotted as a function of $g_0 c(= 2\pi c/\gamma\lambda)$ for various values of c/a.[19]

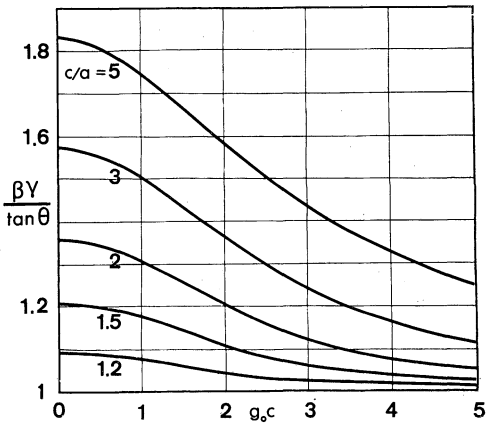

FIG. 2. Phase velocity of a single sheath helix waveguide as a function of $g_0 c$ for several values of c/a.

As mentioned above, this model cannot accurately represent the field distribution near the helix, nor can it give the actual losses. The tape model improves the situation with respect to the fields, but still cannot give the losses, since an infinitely thin tape is completely different from a real wire. The tape helix analysis, which agrees with experimental results, shows[21] that the periodicity of the helix becomes important to the propagation characteristics only at frequencies much higher than those of interest for accelerator applications; additional modes begin to propagate at high frequencies and large pitch angles. These higher modes can be eliminated by introducing additional helix wires between the coils, giving a closer approximation to the sheath helix.

With the sheath helix model, one may estimate which field components will be largest near the conducting surfaces. The largest magnetic field component for $c/a \gtrsim 1.5$ is $B_z^i(a)$, just as in a solenoid. $E_r^o(a)$ is the largest electric field. These

field levels are shown in Figs. 3 and 4 as a function of $g_0 c$ for various values of c/a. The values of $B_z^0(a)$ and $B_r(a)$ are important when considering losses and large wires. They are shown in Figs. 5 and 6. The ϕ components of both E and B fields are very small for $v/C \ll 1$. The variation of the large field components with radius is shown in Fig. 7.

B. *Corrections to the Sheath Model*

The solutions given so far have been for traveling waves. The power in these waves is of the order of megawatts for accelerating fields greater than about 1 MV/m. Therefore, it appears that a standing wave configuration would be more practical for an accelerator. Because of the mixed TE–TM character

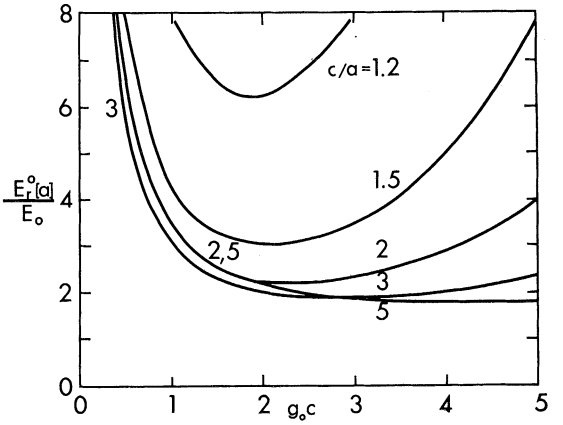

FIG. 3. Radial electric field at the outside of the sheath helix as a function of $g_0 c$ for several values of c/a.

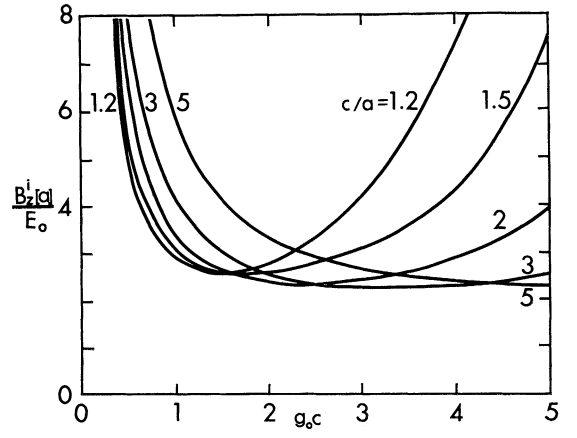

FIG. 4. Axial magnetic field inside the sheath helix as a function of $g_0 c$ for several values of c/a.

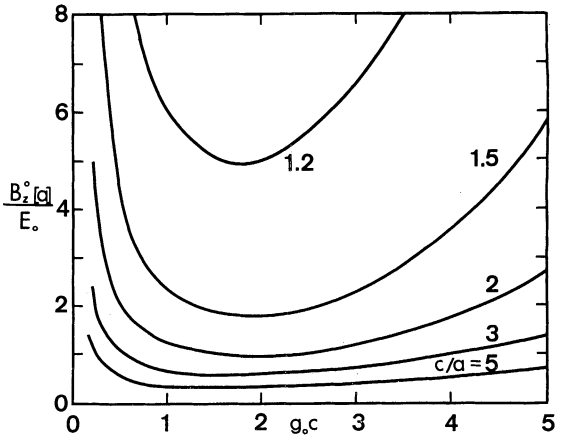

FIG. 5. Axial magnetic field outside the sheath helix as a function of $g_0 c$ for several values of c/a.

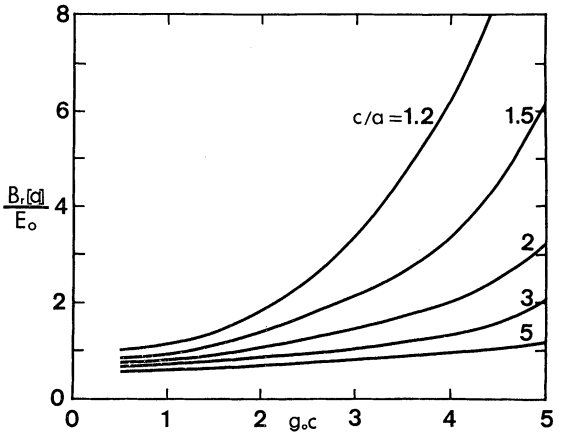

FIG. 6. Radial magnetic field at the sheath helix as a function of $g_0 c$ for several values of c/a.

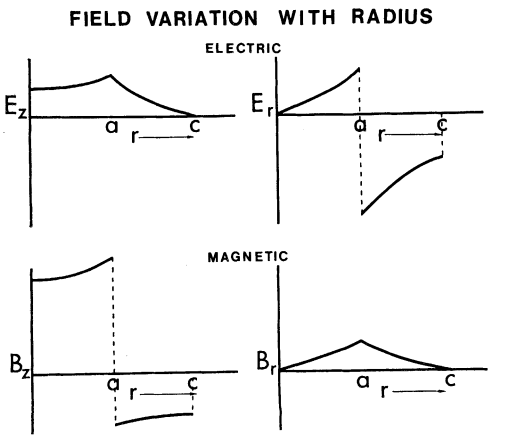

FIG. 7. Variation of the large field components with radius in the sheath helix (schematic).

of the wave, a shorting plane across a helical waveguide does not correctly satisfy the boundary conditions for a pure standing wave. There will be an unavoidable distortion of the magnetic fields in the TE portion of the wave, but there is little effect on the TM (accelerating) part of the wave. The main effect for our consideration is a frequency shift from a predicted value of $\nu_{m'} = m'v(\nu)/2L$ for an $m'\lambda/2$ standing wave cavity of length L. This effect cannot be quantitatively predicted theoretically at this time. This shift was observed to be less than 3 per cent in an actual 2λ helical resonator.

The main modification to the sheath model given here is to include finite wires, allowing the accurate prediction of losses. There are two important effects of the wires. The radial electric field is increased locally due to the finite radius of curvature of the wires. This effect increases B_z by a similar factor. There is an enhancement of B_r caused by flux conservation in the smaller area available between the large wires. This effect also increases the E_z field between the wires by the same factor.

Since the first effect becomes smaller for larger wires, while the second increases, there will be some value of d/p which causes the magnetic fields at the wire from both effects to be equal.

Appendix B gives the details of the conformal transformation which was used to estimate the magnitude of the fields at the conductors in terms of the sheath model values. These calculations result in factors which must multiply the sheath helix fields to give a more accurate estimate. Figure 8 gives these factors as a function of d/p.

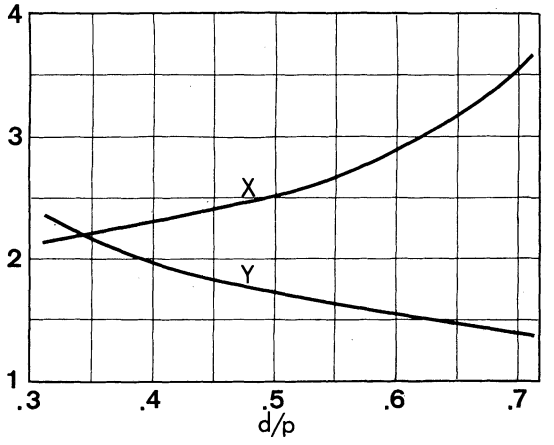

FIG. 8. Correction factors to sheath helix fields due to large wires as a function of d/p. X multiplies B_r and E_z, Y multiplies E_r and B_z.

X is the factor which multiplies E_z and B_r, while Y is the factor for B_z and E_r.

These field mappings also lead to values of the surface current density in the wires; knowing these currents allows a calculation of losses in the helix. This calculation also is done in Appendix B. The losses in a standing wave cavity with $d/p = 0.6$ are shown in Fig. 9. Figure 10 shows the fraction of losses occurring in the outer shield for such a cavity. These curves are valid for $(v/C)^2 \lesssim 0.2$.

4. MECHANICAL PROPERTIES OF THE HELIX

From the considerations mentioned in Sec. 2, it will probably not be possible to introduce any

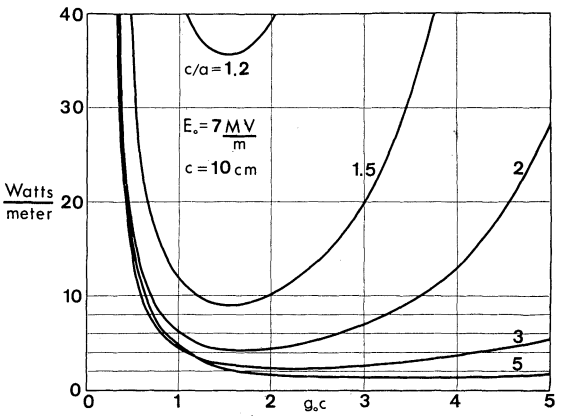

FIG. 9. Losses in a single helix cavity with $d/p = 0.6$ as a function of g_0c for several values of c/a. Magnitudes are for $E_0 = 7$ MV/m, $R_s = 10^{-8}\ \Omega$, $c = 10$ cm. Losses scale as $cR_sE_0^2$.

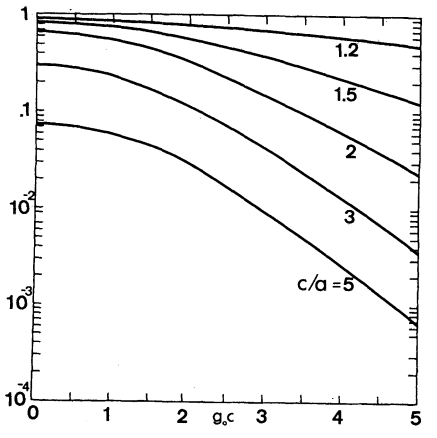

FIG. 10. Fraction of the losses of Fig. 9 occurring in the outer shield, as a function of g_0c, for several values of c/a.

dielectric supports into a superconducting helical accelerator. The structure would necessarily consist of a long helix supported only at voltage nodes by superconductors, or of a series of separate half-wave sections. Because of the necessity of cooling, the helix should be formed of a hollow tube. Below we consider limits on the unsupported length of a helix. The actual calculations are given in Appendix C.

The compressional modulus under small deformations for a spring wound from a hollow tube is

$$K = \frac{\pi\mu d^3 \Delta d \sin\theta}{8a^2} \qquad \left(F = K\frac{\Delta z}{z}\right). \tag{6}$$

The amount of sag due to gravity for such a structure is

$$\delta = -\frac{\rho g \mathscr{L}^4 \eta}{48\mu d^2 \sin^2\theta}, \tag{7}$$

where η is a factor of order 1, which depends on the 'effective moment of inertia' of the helix; $\eta = 4$ for a solid bar, and $\eta = 2$ for a thin-walled pipe. For a copper helix with $d = 1$ cm, $\theta = 0.08$, a deflection of 1 mm occurs for $\mathscr{L} \cong 22$ cm.

Since a small static sag has a negligible effect on the accelerating fields and on losses, static gravitational deformation will not be the most troublesome problem.

At the energy gradients considered, there are magnetic fields of from 50 to 500 gauss acting on the helix, in which there are large currents. In addition, the electric fields also lead to comparable forces. The longitudinal force acting per centimeter of helix is

$$\frac{dF_z}{dz} \cong \frac{0.06a}{\cos\theta}(B_r B_- + E_z E_-)\sin\frac{4\pi z}{\lambda}\frac{\text{dyn}}{\text{cm}}. \tag{8}$$

(There is also a force acting radially on the coils, but the deformation caused by this force is much smaller, so the frequency effects are small.) This force is an average over times short compared to mechanical vibration frequencies; it produces a static 'strain wave' which is linear in the field energy. The pitch of the helix is distorted to

$$p = p_0 + \Delta p \cos\frac{4\pi z}{\lambda}, \tag{9}$$

where

$$\frac{\Delta p}{p} \cong \frac{0.06a}{K\cos\theta}\frac{\lambda}{4\pi}(B_r B_- + E_z E_-). \tag{10}$$

One may estimate the frequency shift in a standing-wave resonator by calculating the effective velocity of a traveling wave in a structure with this perturbed pitch. This shift is

$$\frac{\Delta v}{v} \cong -0.5\left(\frac{\Delta v}{v}\right)^2, \tag{11}$$

where

$$\frac{\Delta v}{v} \cong \frac{\Delta p}{p}\frac{1}{1+g_0 cf'/f}. \tag{12}$$

For the helix given under Eq. (7), $\Delta v/v \sim -1\times10^{-5}$ for an energy gain of 3 MeV/m.

5. PHASE SPACE AND FOCUSING

If a collection of particles is assumed noninteracting, the motion of the members of that collection is limited by Liouville's theorem. Liouville's theorem states that if the particles are under the influence of forces derivable from a Hamiltonian, which is always true of electromagnetic forces, then the volume they occupy in phase space is conserved. Phase space is a six-dimensional space whose coordinates are the canonical coordinates and momenta of the Hamiltonian.[23] In addition, if the change in one coordinate is coupled only weakly to the others, areas in the three orthogonal two-dimensional spaces of coordinates with conjugate momenta are separately conserved. Thus, it is useful to study the effect of an accelerating or focusing system upon a group of particles by examining the change of shape of phase space areas. The effect of coupling between coordinates (e.g., E_z is a function of r) is to cause different behavior of the (q_i, p_i) phase-space plane for different values of q_j and p_k $(j, k \neq i)$, while preserving the total six-dimensional volume. The effect of space charge is to increase the total phase-space volume.[23]

Focusing in linear accelerators may be examined with the aid of the phase-space concept. It is common when discussing linear accelerators to consider a focused system as one having stable, bounded motion in phase space, as opposed to the optical meaning of reducing the spatial dimensions of a beam. Thus, one speaks of radial and longitudinal focusing, which means that the particles move on closed, bounded surfaces in phase space, and all particles initially located inside of one of these surfaces remain enclosed.

In the usual heavy ion accelerator, longitudinal stability is achieved by the 'surfrider principle'. The machine is designed so that the velocity of the accelerating wave is equal at all times to the instantaneous velocity of one particle. The phasing is such that the particle is on the forward side of the

wave, so that leading particles see a smaller field, and trailing particles see a larger field. Thus, particles away from the equilibrium phase feel a restoring force toward that point.

Depending upon the chosen value of the stable phase, different fractions of a dc beam are trapped and accelerated. The usual method is to use a stable phase point about 30° in advance of the wave crest. Twenty-five per cent of a dc beam is trapped in a stable region by this design. In Fig. 11, the longitudinal phase-space trajectories of particles in this type of accelerator are shown.

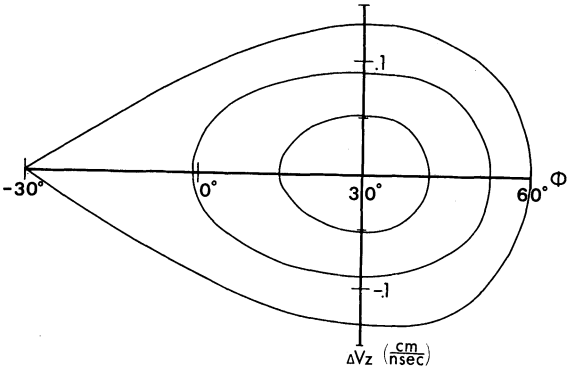

FIG. 11. Longitudinal phase space curves for non-relativistic protons in a standing-wave accelerator with $E_0 = 10$ MV/m, $\lambda = 40$ cm, and $\phi_s = 30°$.

In a high-gradient accelerator of this design, the problem of energy spread becomes important. For example, for an accelerator with $E_0 = 10$ MV/m, $\lambda = 40$ cm, and $\phi_s = 30°$, a pulse of 50 MeV protons of full $\lambda/4$ length will have an energy spread of about $\Delta\epsilon/\epsilon \sim 0.03$.

There are two ways to improve energy resolution with a fixed field strength and wavelength. One may restrict the phase width of the particle bunch, or operate at a smaller stable phase angle. By reducing ϕ_s to 5°, one gets the stable trajectories shown in Fig. 12. The longest pulse that may be trapped is now 4 per cent λ, and a 2 per cent λ pulse at 50 MeV has $\Delta\epsilon/\epsilon = 0.002$, with the same E_0 and λ as before. This value of $\Delta\epsilon/\epsilon$ could be reduced only by decreasing the accelerating field.

It was shown by McMillan[24] that for charge-free regions of electric field, a particle bunch can be focused in only one dimension if it has a constant stable phase point. Therefore, an accelerator operated in the above manner is unstable in the radial direction, and will not radially focus a beam. Conversely, for a stable phase trailing the wave crest, the beam is stable radially, but diverges

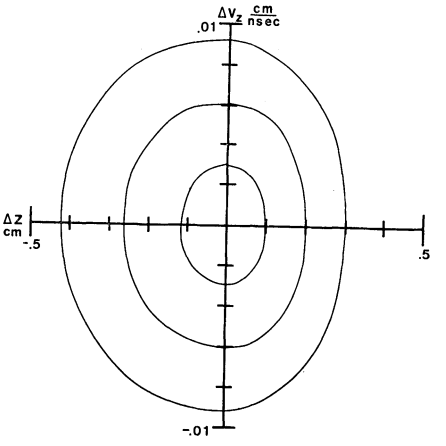

FIG. 12. Longitudinal phase space curves for non-relativistic protons in a standing wave accelerator with $E_0 = 10$ MV/m, $\lambda = 40$ cm, and $\phi_s = 5°$.

longitudinally. This difficulty is overcome by using external focusing devices such as alternating-gradient quadrupoles or electric field grid focusing.[5] This adds to the complexity of an accelerator, and the use of large magnetic fields near a superconductor causes difficulties.

McMillan's proof is valid only if the central phase of the bunch remains a constant. It was soon proposed to use a varying phase; with the bunch alternating between regions of radial and longitudinal stability, net stability in both directions would result, in analogy to the strong focusing principle.[25–27]

This proposal was discarded because numerical computations[25–28] showed that the phase acceptance was limited to a few degrees. However, when one considers the problem of energy spread mentioned above, and the better bunching techniques presently available, one realizes that the limited phase acceptance may not be impractical. The desire not to have magnetic quadrupoles near superconductors also makes this type of focusing more attractive for superconducting linacs.

All of the above work on alternating phase focusing used the idea of externally varying the phase. This calls for a continuous or nearly continuous varying of the wave velocity in the structure (modifying drift tube lengths, dephasing cavities, etc.).

6. THE SLINGSHOT

The desired result may be produced in a much simpler fashion; by utilizing the phase changes

caused by the particles' acceleration in a constant velocity wave, it is possible to achieve simultaneous radial and longitudinal stability.

The procedure is as follows: the bunch enters the accelerator section with a lower velocity than the wave, with an initial phase of from 50° to 90° leading the wave crest. It passes backward through the region of longitudinal focusing and radial defocusing to the rear of the wave crest, where the opposite conditions exist. Since the particles are being continuously accelerated by the wave, their velocity equals that of the wave at a point from 25°–40° behind the crest. The acceleration continues until the bunch reaches the approximate phase of entry, at which point the accelerator section is terminated, and the bunch may enter another section that has a higher wave velocity.

In the reference frame of the traveling wave, the acceleration process is like that of a stone hitting an elastic band and rebounding. Hence, the term 'slingshot'. The effect of this procedure is analogous to that of passing through an alternating-gradient triplet lens, for both radial and longitudinal motion, but it also involves an acceleration. The actual average energy gain is 85 per cent to 95 per cent of the electric field amplitude in the traveling wave, with the value depending upon the initial phase point. For accelerating fields of the order of 1–5 MV/m, only a small number of these constant velocity sections is needed. The velocity increment of one section is of the order of 0.02 C to 0.07 C (in the wave frame).

The behavior of particles in this type of self-focusing wave has been calculated for a variety of e/m values, field strengths, and velocities.

The particle motions were studied by numerically integrating the non-relativistic equations of motion for charged particles in the complete electric and magnetic fields for a sheath helix standing-wave cavity—neglecting the fringing fields at both ends. The trajectories were computed in the frame of the moving wave. Since the largest velocities encountered here are < 0.05 C, these equations are quite accurate. However, the results are not limited to low velocities in the laboratory, since they may be Lorentz-transformed from the wave to the laboratory frame, as the relativistic effects on the backward traveling wave were accounted for in the wave-frame calculation.

By calculating the final positions of particles initially scattered in phase space, it was possible to determine the phase trajectories of particles passing through the 'slingshot'. In this manner, acceptance curves in longitudinal and radial phase space were obtained. These results are shown in Figs. 13 and 14.

The detailed shape of the phase space curves depends upon the initial and final phases, and velocities. Curves with larger velocity spread may be obtained by varying the entering and exiting phase slightly. This may be desirable for a low velocity, low field accelerator because of bunching criteria.

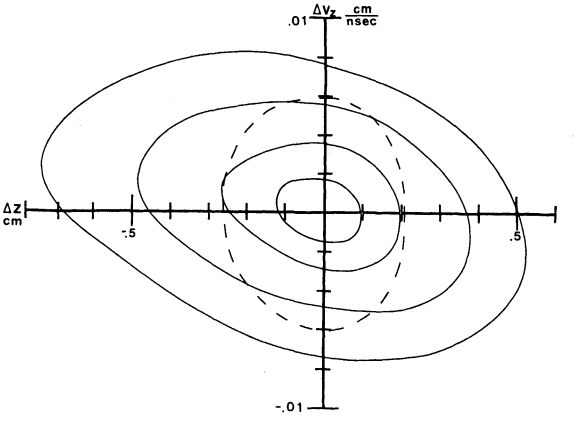

FIG. 13. Longitudinal phase space curves for non-relativistic protons in a standing wave 'slingshot' accelerator with $E_0 = 10$ MV/m and $\lambda = 40$ cm. The dotted curve is a phase space region from the stable phase accelerator of Fig. 12, showing the large improvement in energy resolution possible with the slingshot.

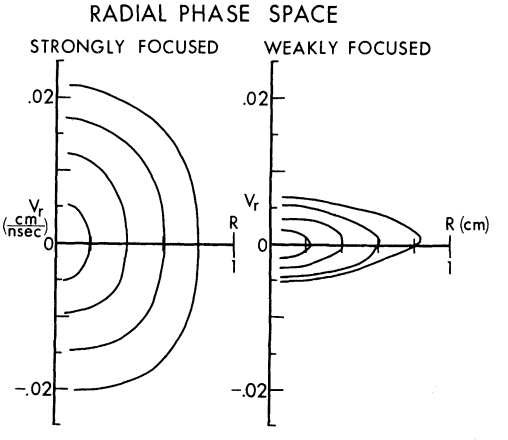

FIG. 14. Radial phase-space curves for non-relativistic protons in a standing-wave 'slingshot' accelerator, with $E_0 = 10$ MV/m and $\lambda = 40$ cm. The 'strongly focused' curves are from one end of a 3.5 per cent λ pulse, with the 'weakly focused' curves from the other end.

The qualitative behavior of the particles is similar for a wide range of e/m values and field strengths. The velocity gain in one section scales with $(eE_0\lambda/m)^{1/2}$, as would be the case if the accelerating wave amplitude were a constant in space instead of a cosine. Calculations were done for values of e/m from 0.02 to 1, λ from 20 to 150 cm, with $E_0 = 10$ MV/m.

Some of the advantages of this accelerating method are:

(1) Each section has a constant phase velocity, which simplifies construction.

(2) Because of the time spent in the longitudinal defocusing region, there is a smaller energy spread for a given pulse length than is possible for a stable-phase accelerator. Figure 13 has one curve from Fig. 12 (shown as a dashed line) superimposed, showing that the velocity spread for a slingshot is about one half the lowest possible value for a stable phase accelerator with the same energy gain.

(3) No separate focusing devices are needed.

(4) The initial particle velocity is lower than that of the wave, so that one can accelerate particles with lower velocities than that of the accelerating structure.

(5) Because of the uniform fields of the low frequency helical cavity, one can accept large radial phase-space areas. For a 1 per cent λ pulse in the strong focusing case of Fig. 14, a 1 cm diam pulse of 500 keV protons with emittance 7π cm-mrad can be accepted, with large diameter pulses limited only by the apertures used.

(6) The procedure is basically a rather weak focusing method, in comparison to presently used methods. Because of this, there are no high frequency oscillations in the radial motion which might cause instabilities. In a 500 ft accelerator taking protons from 500 keV to 700 MeV, particles might cross the axis 4 to 6 times.

(7) One may vary the output energy of this type of accelerator over a continuous range by varying the field level simultaneously with the relative phasing. If the field amplitude of the last section is held at 70 per cent of the design level, and the particles' initial phase changed to about 180°, they slip back by about $1\frac{1}{2}$ waves, and exit with the same velocity with which they entered. The radial and longitudinal phase-space properties of the section operated in this manner are nearly the same as when accelerating. For the intermediate field levels, the energy spread of the exiting beam increases to a maximum of about eight times the original value when the final velocity is equal to the wave velocity. This spread could be counteracted by the use of a 'bunching section' after the final accelerating section. The actual result would be a debunching, but a buncher field profile would provide the desired effect. The radial phase space quality is also worsened by a moderate amount. At 50 MeV the emittance of a 1 cm diam beam at the full acceleration is 0.75π cm-mrad. Exiting at the wave velocity of the last section, the beam is about 0.9 cm across, with an emittance of about 1.2π cm-mrad. Of course, the emittance does not need to be this large, if the initial emittance is reduced, or if the accelerator is operated in a more weakly focusing manner.

There are several limitations on this accelerating method. The focusing produced by the slingshot is quite astigmatic; the limitations on the pulse length trapped are due to radial defocusing at either end. Figure 14 shows the radial phase-space curves at the opposite ends of a pulse of length $0.035\,\lambda$. Five per cent of λ (18°) appears to be the maximum pulse length trapped by this method. For 50 MeV protons with $\lambda = 40$ cm, and $E_0 = 10$ MV/m, a 4 per cent λ pulse corresponds to $\Delta\epsilon/\epsilon \cong 0.002$. A 1 per cent pulse gives 6×10^{-4}; $\frac{1}{2}$ per cent gives 3×10^{-4}.

This type of accelerator is also necessarily designed for a single velocity profile. Different particles may be accelerated in a single machine by varying E_0 to keep $E_0 e/m$ constant. However, the maximum field level must be chosen for the smallest e/m, thus limiting the energy gain of ions of larger e/m. This difficulty could be overcome for a superconducting accelerator, for which a large part of the cost is the dewar and refrigerator system, by having two or more accelerating structures inside the dewar, each for a certain range of e/m values. All existing linear accelerators have this limitation on e/m range, but there have been proposals made which would allow acceleration of all possible ion types with optimum energy gain for each.[29,30]

7. THE DOUBLE HELIX WAVEGUIDE

The single helix waveguide already discussed is limited to use at $\beta \gtrsim 0.04$. Because of the stiffness criteria discussed in Sec. 4, a smaller pitch implies a smaller wire size, which results in a structure too unsteady to be practical.

By adding an additional helical conductor of radius b coaxial with the first ($a < b < c$), one

increases the capacitance and inductance of the structure, lowering the phase velocity by a useful amount. In Appendix D is presented a mathematical analysis of the double helical transmission line in the sheath approximation. Experiments indicate that the sheath model predicts the dispersion properties of the double helix as well as it does those of the single helix. Some of the results of the calculations are discussed here.

Since there is a third conductor present in the system, there is a splitting of the modes, one wave propagating more slowly than for a single helix, and one more rapidly. There are four distinct modes possible in this structure, the additional two resulting from the possibility of even or odd relative parity of the two helices.

When both helices are wound with the same parity, the additional helix exerts a relatively small perturbing effect. One mode is a propagation of the basic single helix wave along one conductor, while the second mode is a propagation along the other conductor. One may achieve slightly lower field levels near conductors with this configuration, but the phase velocity is about the same as in the single helix. The extra complexity of this structure is not worth the marginal improvement gained.

Both modes of the cross-wound, double helix waveguide appear to be interesting for use as particle accelerators. The field lines in these modes are indicated in Fig. 15. It is clear that the field distributions are not simply perturbations of those of the single helix.

The slow mode has higher field levels than the single helix; this is the price of achieving a lower phase velocity. The largest magnetic field in this mode, assuming reasonable spacings between the helices and the outer shield, is $B_z^i(a)$. This is the largest component over the entire ranges of Figs. 16, 17, and 18. The maximum electric field, usually of nearly the same magnitude as $B_z^i(a)$, is $E_r^0(a)$. The currents in the two helices are of opposite polarity, causing a large electric field between them.

From the numbers mentioned in Sec. 2, it appears that minimization of B field is of primary importance. $B_z^i(a)$ is proportional to $E_0(t_a/\beta)(I_{0a}^2/I_{1a})$ (see Appendix D, Eq. (D.4), row 5). The function I_0^2/I_1 has a minimum of 2.71 at $g_0 a = 1.29$, but is within 5 per cent of this value for $1.1 \leqslant g_0 a \leqslant 1.6$. Any convenient arrangement of b, c, and t_b/t_a which gives the desired velocity ratio, and reasonable maximum electric fields may be used. With a fixed maximum field, the energy gain will drop linearly with the value of $\beta/\tan\theta_a$ achieved.

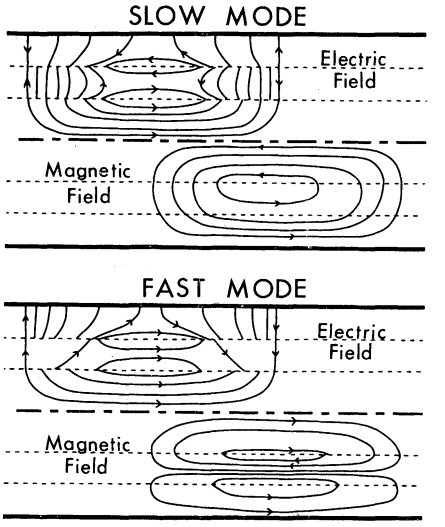

FIG. 15. Field lines in the modes of the cross-wound double helix waveguide. In each picture, the upper half shows the electric field, and in the lower half the magnetic field, with the correct phase relation for a traveling wave.

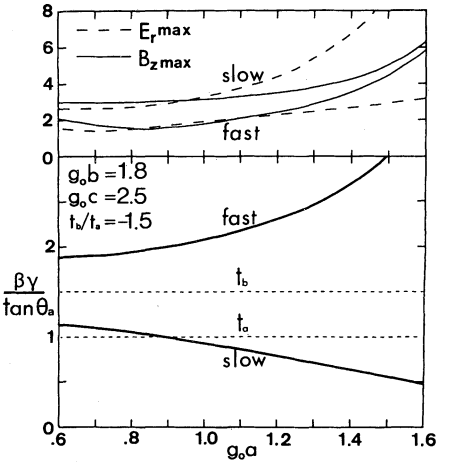

FIG. 16. Dispersion curves and maximum field levels (in terms of E_0) for a cross-wound double helix with $g_0 a$ varying. Dashed lines show $\beta = \tan\theta$.

The fast mode has currents of the same polarity in both helices. This results in a large magnetic field between the helices, and a large electric field between the outer helix and the shield (see Fig. 15). A minimum magnetic field much lower than possible in the single helix may be achieved by varying the position of a and b to cause $B_z^i(a)$ to equal $B_z^0(a)$ or $B_z^i(b)$. In this case, all four of the important independent parameters of the double helix, $g_0 c$, $g_0 b$, $g_0 a$, and t_b/t_a affect the result.

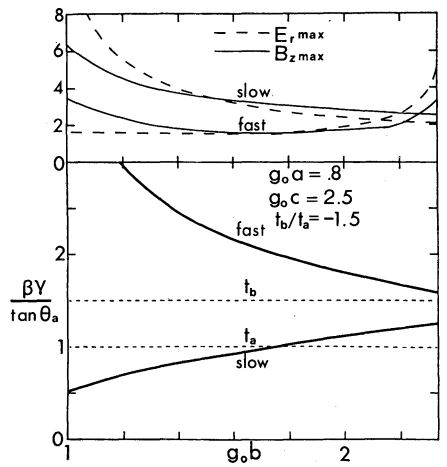

FIG. 17. Dispersion curves and maximum field levels (in terms of E_0) for a cross-wound double helix with g_0b varying. Dashed lines show $\beta = \tan\theta$.

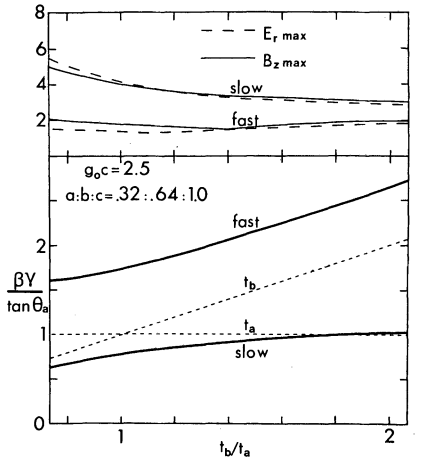

FIG. 19. Dispersion curves and maximum field levels (in terms of E_0) for a cross-wound double helix with t_b/t_a varying. Dashed lines show $\beta = \tan\theta$.

Figures 16, 17, 18, and 19 show how the dispersion curves and maximum fields for both modes vary with the four parameters. The dashed lines shown with the dispersion curves give the velocities that waves propagating at C along the helix wires would have. The constant parameters in each of the four figures were chosen to give low fields in the fast mode. The slope discontinuities in the curves occur when a different field component becomes the maximum (see $g_0b = 2.2$ in Fig. 17). As can be seen from the figures, there is quite a broad minimum in the field levels. A large range of c/a, c/b, g_0c and t_b/t_a give $B_{max}/E_0 \leqslant 1.60$; the lowest value of this ratio found was $B_{max}/E_0 = 1.50$ for $g_0a = 0.77$, $g_0b = 1.77$, $g_0c = 2.75$, and $t_b/t_a = -1.65$. The phase velocity ratio for this configuration is: $\beta/t_a = 2.1$. These numbers compare very favorably with those of the single helix, where the minimum of B_{max}/E_0 is 2.3 for $c/a = 2$ (see Fig. 4).

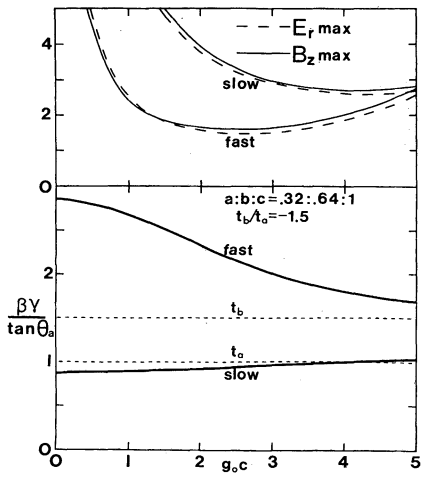

FIG. 18. Dispersion curves and maximum field levels (in terms of E_0) for a cross-wound double helix with g_0c varying. Dashed lines show $\beta = \tan\theta$.

The radial magnetic field will be important, of course, as in the single helix; this can be calculated from $B_r = (t/\beta)E_z$ at any helical sheath.

For any specific geometry, optimum wire size may be calculated using Fig. 8, and losses may be found with the aid of Eq. (B.5) in Appendix B, once the sheath model has been solved.

The slow mode of the double helix waveguide allows traveling waves of $\beta \approx 0.01$, which makes possible, using the slingshot, the acceleration of very low velocity particles—such as protons from a low voltage source, or very heavy ions from a high voltage dc source. Also, the fast mode allows a significant (50 per cent) improvement in energy gain over the single helix in the velocity region $\beta \gtrsim 0.10$.

8. DESIGNING ACCELERATORS

In this section, it will be shown how the various graphs and data presented in this paper may be used to make fairly accurate first order approximations to accelerator designs.

It is most instructive to do this by means of an example. Consider an accelerator which is to accelerate protons from a 500 keV source. Assume that a material with $(H_c)_{ac} = 500$ Oe is available, and that a maximum electric field of 30 MV/m is allowed. Because of cooling considerations, the entire structure is limited to 20 cm diameter. The velocity gain in one slingshot section is, for all cases:

$$v_f - v_i \cong 2\left(\frac{e}{m}\frac{E_0}{10}\frac{\lambda}{40}\right)^{1/2}\frac{\text{cm}}{\text{nsec}}, \tag{13}$$

where $e/m = 1$ for protons, E_0 is in MV/m, and λ in cm. The acceleration is such that

$$\frac{v - v_i}{v_f - v_i} = 0.55, \qquad \frac{v_f - v}{v_f - v_i} = 0.45. \tag{14}$$

Estimating $E_0 = 4$, $\lambda = 30$, we find from Eq. (13) that $\beta \cong 0.05$.

A number of criteria for maximum unsupported length may be used. We shall require that gravitational sag be less than 1 mm. From Sec. 4 this implies

$$\frac{\mathscr{L}^4}{d^2 \sin^2\theta} \lesssim 5 \times 10^7 \text{ cm}^2. \tag{15}$$

There are two possibilities for the structure. Either a slow mode double helix, which would have a lower energy gain, or a single helix may be used. We would prefer the single helix, but will have to avoid the problem of tight pitch requiring too small wires. Maximizing the pitch for fixed c would imply small c/a.

Since the B field will be the limiting factor on energy gain, we choose $c/a = 1.5$, since this is the smallest value where $B_z^0(a) \lesssim B_z^i(a)$. With $\theta \sim 0.045$ (from Fig. 2), the pitch will be $2\pi a \tan\theta \sim 1.9$ cm. This pitch gives $d/p \sim 0.66$ for 13 mm diam. helix wires.

From Eq. (15) we find $\mathscr{L}_{\max} = 18$ cm. With $\lambda = 36$ cm, $g_0 c = 1.75$. From Figs. 4, 6, and 8, the magnetic field will be: $B_z^i(a) = 3.7E_0$, $B_r(a) = 4.2E_0$. The 500 Oe limit implies $E_0 \cong 3.6$ MV/m.

The revised value of $E_0\lambda$ leads to $v - v_i = 0.620$ cm/nsec, which gives $\beta = 0.053$. The pitch is corrected to $41.9 \times 0.053/1.125 = 1.99$ cm; d/p is now 0.64.

This approximation procedure may be continued until the various results are self-consistent to the desired accuracy. For this example, the resulting structure has the specifications:

$c = 10$ cm, $\quad a = 6.7$ cm,

$\lambda = 36$ cm, $\quad p = 2.0$ cm,

$B_z^i(a) = 3.7E_0$, $\quad B_r(a) = 3.9E_0 = 500$ G,

$E_0 = 3.9$ MV/m $= 130\ st\text{-}V$/cm

$v_i = 0.98$ cm/nsec, $\quad \epsilon_i = 500$ keV,

$v = 1.62$ cm/nsec, $\quad v_f = 2.15$ cm/nsec,

$\epsilon_f = 2.4$ MeV, $\quad$ Length $= 108$ cm $= 3\lambda$

$E_{\max} = 12.5$ MV/m, $\quad$ and $\quad \nu = 45$ MHz.

From Fig. 9 we find the losses in the cavity (assuming no dielectric losses) to be 2.8 $(R_s/10^{-8})$ W/m.

Dimensions of the following sections may be estimated by the same procedure, with the additional restriction that their frequencies must be integer multiples of the frequency of the first section. For this specific example, the next section would possibly be a fast mode double helix, because of the increased energy gain possible.

9. CONCLUSION

This paper has dealt with the possibility of using a superconducting helical waveguide as a heavy particle accelerator. Methods are given for accurately estimating maximum field levels, losses, various distortions, and frequency shifts. Two new results are presented: the analysis of the double helix waveguide†; and the slingshot method of simultaneous radial and longitudinal focusing by self-phasing.

The question of whether this type of accelerator is practical depends upon a number of unanswered experimental questions. Whether the energy gain achievable will be competitive depends upon what value of the ac magnetic field can be tolerated by the superconductor in long-term use. The surface resistance at these low frequencies must be low enough so that the losses are tolerable (see Fig. 9). Methods of automatic tuning must be developed that can operate over a range of $\Delta\nu/\nu \sim 10^{-5}$ when Q values are 10^9–10^{10}.

The analysis suggests that if the above-mentioned problems are solved the single helix may be practical as an accelerator for velocities from $\beta \cong 0.05$ to $\beta \cong 0.15$. The double helix may be used from $\beta \cong 0.01$ in the slow mode to $\beta > 0.5$ in

† Since performing these calculations, the authors have learned that the double helix was analyzed in unpublished work by W. B. Hebenstreit at the Bell Telephone Laboratories in 1946–1947. He constructed a traveling wave electron tube amplifier in which the electrons traveled between the two coils.

the fast mode. The use of the slingshot effect will allow ions with initial velocities $\beta \lesssim 0.01$ to be accelerated in these structures.

The ultimate success of the slingshot method will depend upon the development of efficient bunchers which can provide a very small bunch with little energy spread.

All the results of the analysis of the helical waveguide are also valid for normal conducting metals. It may be practical to utilize the low phase velocity of the double helix to construct traveling wave bunchers for protons, or accelerators for very heavy, low-energy ions, made from normal materials.

ACKNOWLEDGMENTS

The authors wish to thank Dr. G. J. Dick for his help in testing the helical resonators and M. Warrick and G. Santantonio for their construction. We also wish to acknowledge the help given by Professor H. A. Schwettman, Dr. M. S. McAshan, Dr. V. Nguyen, and Mr. M. N. Kronick of Stanford University in providing both experimental and theoretical results in advance of publication.

APPENDIX A

Glossary of Symbols

a	radius of inner helix.
a_1	numerical constant used in conformal mapping, Appendix B.
b	radius of outer helix.
b_m	axial wave number of mth mode.
b_0	axial wave number of traveling wave. $b_0 = 2\pi/\lambda = \omega/v$.
c	radius of outer shield.
d	diameter of helix wire.
Δd	wall thickness of tubing used for helix.
e/m	charge to mass ratio of particle.
$f(g_0 c)$	dispersion function for single helix. $f(g_0 c) = \beta\gamma/\tan\theta$.
g	gravitational acceleration.
g_m	radial wave number of the mth mode.
g_0	radial wave number of helix wave. $g_0 = b_0/\gamma = (b_0^2 - k^2)^{1/2}$.
k_B	Boltzmann's constant.
k	free space wave number. $k = \beta b_0 = \omega/C$.
m	azimuthal mode number.
m'	standing wave mode number; number of half-wavelengths.
q_i	canonical coordinate of Hamiltonian.
p	pitch of helix.
p_a	pitch of helix at $r = a$.
p_b	pitch of helix at $r = b$.
p_i	canonical momentum coordinate of Hamiltonian.
p_0	unperturbed pitch of helix.
Δp	amplitude of pitch perturbation.
r	radial cylindrical coordinate of helix.
t_a, t_b	$\tan\theta_a$, $\tan\theta_b$; tangent of pitch angle.
δ	loss angle; imaginary part of dielectric constant $= \epsilon \tan\delta$.
v	wave velocity.
v_i	velocity of particles entering a slingshot section.
v_f	velocity of particles leaving a slingshot section.
v_{av}	average velocity of a wave on a helical structure with a perturbed pitch.
Δv	amplitude of velocity perturbation.
w	distributed loading applied to a beam.
x	$ik/g_0 t_a$—see Appendix D.
z	axial cylindrical coordinate of helix.
Z	coordinate of the complex plane of the large wire grating (Appendix B).
z_1	coordinate of the half-plane mapped into the large wire grating.
Δz	distortion of helix under longitudinal force.
B	magnetic field.
$B_\parallel$	component of B parallel to a conductor.
$B_\perp$	component of B perpendicular to a conductor.
B_z^m, B_r^m, B_ϕ^m	magnetic field component of the mth azimuthal mode.
B_z^i, B_z^0, B_r	sheath helix values for B components at a conductor. Superscript tells if inside or outside of a sheath.
$B_\pm$	$(B_z^0 \pm B_z^i)/2$.
C	velocity of light.
C_0	capacitance per unit length.
ϵ	energy of particle.
E	electric field.
$E_\parallel$	component of E parallel to a conductor.
$E_\perp$	component of E perpendicular to a conductor.
E_z^m, E_r^m, E_ϕ^m	components of E in mth azimuthal mode.

E_z, E_r^0, E_r^i sheath helix components of E at a conductor. Superscript tells if inside or outside of a sheath.

E_0 amplitude of standing wave. Amplitude of accelerating component is $E_0/2$. Energy gain is $\sim 0.45E_0$.

$E_\pm$ $(E_r^0 \pm E_r^i)/2$.

ϵ_i initial energy of particle.

ϵ_f final energy of particle.

$\Delta\epsilon$ energy spread of beam.

$F_z(z)$ tensile force acting in the helix.

$$F_z(z) = \int_0^z \frac{dF(z')}{dz'}\,dz'.$$

$\frac{dF_z(z)}{dz}$ longitudinal applied force density; dynes/cm of helix.

H_c critical magnetic field of a superconductor.

J_ϕ current density in helix wire.

K spring constant of helix; $F = K\Delta z/z$.

I_m, K_m modified Bessel functions of order m.

I_{0a}, K_{0c}, etc. $I_0(g_0 a)$, $K_0(g_0 c)$, etc.

L, M, N Fourier components of approximate current distribution in helix wire.

L_0 inductance per unit length.

$\mathscr{L}$ distance between the supports of a helix. $\mathscr{L} = \lambda/2$.

$\mathscr{M}(z)$ bending moment in a beam.

P power loss per cm of helix.

Q quality factor of cavity.

$R(g_0 r)$ $I_0(g_0 r) - (I_{0c}/K_{0c})K_0(g_0 r)$.

$S(g_0 r)$ $I_0(g_0 r) + (I_{1c}/K_{1c})K_0(g_0 r)$.

$T(g_0 r)$ $I_1(g_0 r) + (I_{0c}/K_{0c})K_1(g_0 r)$.

$U(g_0 r)$ $I_1(g_0 r) - (I_{1c}/K_{1c})K_1(g_0 r)$.

T absolute temperature.

U ReW.

V ImW.

W complex potential function (see Appendix B).

X field enhancement factor for B_r and E_z.

Y field enhancement factor for B_z and E_r.

$\mathscr{Y}$ Young's modulus (Appendix C).

β v/C.

γ $1/(1-\beta^2)^{1/2}$.

$\delta(z)$ sag of helix.

ϵ_g energy gap of a superconductor.

ϵ real part of dielectric constant.

η numerical factor;

$$\eta = \int dA / \int (r/a)^2 \sin^2\theta\, dA.$$

θ pitch angle; $\tan\theta = p/2\pi a$.

θ_a, θ_b pitch angle of the sheaths at a and b.

λ wavelength.

μ shear modulus.

ν frequency of wave.

$\Delta\nu$ frequency shift.

ξ numerical constant used in conformal mapping, appendix B.

ρ mass density of helix tubing material.

σ perpendicular stress component on helix wire due to fields.

ϕ azimuthal cylindrical coordinate of helix.

ϕ' angular coordinate in the helix wire (Fig. B.1).

ϕ_s stable phase value of constant phase accelerator.

ω radian frequency of wave; $\omega = 2\pi\nu$.

APPENDIX B

Current Distribution in Helix Wires and Losses

B.1. *Current Distribution.* An approximation to the field distribution near the helix wires may be obtained by assuming that the adjacent helix wires form an infinitely long, large wire plane grating. This approximation is valid for distances which are small compared to the radius of the helix. Then, by assuming pseudostatic conditions, a conformal mapping may be used to find the fields. Since the frequencies of interest correspond to free space wave numbers of from 0.002 cm^{-1} to 0.04 cm^{-1}, this is a reasonable approximation for distances of a few centimeters.

The transformation[31]

$$Z = \frac{p}{\pi(1+\xi)}\left[\tanh^{-1}\left(\frac{z_1-1}{z_1+a_1}\right)^{1/2} + \xi\tanh^{-1}\left(\frac{z_1+1}{z_1+a_1}\right)^{1/2}\right], \quad \text{(B.1)}$$

transforms the upper half plane (z_1) into a region in Z extending from the center of the grating at ReZ = 0 to ReZ = ∞, and from the midpoint of one wire (ImZ = 0) to the midpoint of the space between the wires (ImZ = $p/2$). There is a nearly circular quadrant (representing the wire) excluded from the area near the origin, of radius $d/2$. The complex function $W = U + iV$ represents the field lines and 'equipotentials' of various situations:

(1) $W \propto \sin^{-1} z_1$, for which the curves U = constant represent the electric field lines which are equal at a distance to $(E_r^0 - E_r^i)/2$; the curves V = constant are the magnetic field lines corresponding to $(B_z^0 - B_z^i)/2$. This mapping represents a net current or charge in the wire.

(2) $W \propto \sin^{-1}[(2z_1 + a_1 - 1)/(a_1 + 1)]$, for which U = constant, gives E field lines which are asymptotically $(E_r^0 + E_r^i)/2$, and V = constant gives B lines which are asymptotically $(B_z^0 + B_z^i)/2$. This case represents no net charge or current in the wire.

(3) $W \propto \sin^{-1}[(2z_1 + a_1 + 1)/(a_1 - 1)]$; the curves U = constant represent the corrected radial magnetic field, B_r, while V = constant gives the corrected E_z.

The constants a_1 and ξ are found from the following equations:

$$\csc\left[\frac{\pi d}{2p}(1+\xi)\right] = \coth\left[\frac{\pi d}{2p}\frac{1+\xi}{\xi}\right], \qquad \text{(B.2)}$$

and

$$a_1 = \coth^2\left[\frac{\pi d}{2p}\frac{(1+\xi)}{\xi}\right] + \cot^2\left[\frac{\pi d}{2p}(1+\xi)\right]. \qquad \text{(B.3)}$$

The detailed field distribution at the wire surface was calculated for $d/p = 0.70$ and $d/p = 0.35$. This function was represented for the three cases by (see Fig. B.1)

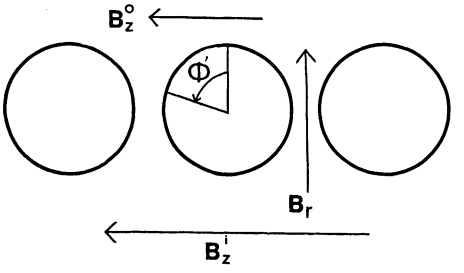

FIG. B.1. Coordinate system for the large wire corrections of Appendix B.

$$\begin{aligned}
(1)\ B_{\phi'}(\phi') &= (M + N\cos 2\phi')B_- \\
E_\perp(\phi') &= (M + N\cos 2\phi')E_- \\
(2)\ B_{\phi'}(\phi') &= L\cos\phi' B_+ \\
E_\perp(\phi') &= L\cos\phi' E_+ \\
(3)\ B_{\phi'}(\phi') &= -X\sin\phi' B_r \\
E_\perp(\phi') &= X\sin\phi' E_z .
\end{aligned}$$

These trigonometric function approximations are valid to better than 2 per cent for $d/p = 0.35$, and within 15 per cent for $d/p = 0.70$. However, the integral of these functions is approximated with much better accuracy. The value of the coefficients L, M, N, and X were calculated for intermediate values of d/p without finding the complete ϕ' dependence. The coefficients L, M, and N are presented in Fig. B.2, and X is given in Fig. 8. The factor $Y \cong M + N$.

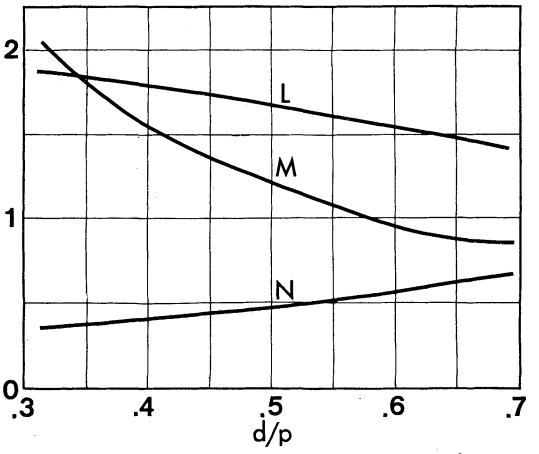

FIG. B.2. Fourier components of approximate surface currents in helix wires as a function of d/p.

Thus, in a standing wave cavity the following surface fields are present:

$$B_{\phi'}(\phi') = [L\cos\phi' B_+ + (M + N\cos 2\phi')B_-]\cos b_0 z \cdot \sin\omega t - X\sin\phi' B_r \sin b_0 z \sin\omega t, \qquad \text{(B.4)}$$

and

$$E_\perp(\phi') = [L\cos\phi' E_+ + (M + N\cos 2\phi')E_-]\sin b_0 z \cdot \cos\omega t + X\sin\phi' E_z \cos b_0 z \cos\omega t. \qquad \text{(B.5)}$$

The quantities B_r and E_z are the sheath helix values, and

$$B_\pm = \frac{B_z^0 \pm B_z^i}{2}, \qquad E_\pm = \frac{E_r^0 \pm E_r^i}{2}.$$

These results are derived for small pitch angles.

B.2. *Losses.* The surface currents in the helix wires are

$$J_\phi(\phi') = \frac{C}{4\pi} B_{\phi'}(\phi'). \qquad \text{(B.6)}$$

The losses per unit length of wire are

$$R_s \frac{d}{2}\int_0^{2\pi} d\phi' J_\phi^2(\phi') = \frac{R_s C^2 d}{32\pi}\{[L^2 B_+^2 + (2M^2 + N^2)B_-^2]\cos^2 b_0 z \sin^2\omega t + X^2 B_r^2 \sin^2 b_0 z \sin^2\omega t\}. \qquad \text{(B.7)}$$

Averaging over time and over a wavelength, the losses per centimeter of helix wire are

$$P = \frac{R_s C^2 d}{128\pi}\{L^2 B_+^2 + (2M^2 + N^2)B_-^2 + X^2 B_r^2\} \text{ ergs/cm} \cdot \text{sec}. \quad \text{(B.8)}$$

$P/\sin\theta$ is the loss in a centimeter of helical waveguide. The loss in the shield is straightforwardly given by

$$P_{\text{shield}} = R_s C^2 \times \frac{(B_z(b))^2}{32\pi} \times c. \quad \text{(B.9)}$$

[The factor $R_s C^2$ in cgs units is equal to $10^9 R_s(\Omega)$.]

The equations (B.8) and (B.9), with the L, M, N, and X values for $d/p = 0.6$ were used to compute the curves given in Figs. 9 and 10.

APPENDIX C

Distortions of the Helix

C.1. *Spring Constant of the Helix.* The torque exerted by a thin-walled tube of length dx in torsion is[32]

$$\tau = 2\pi\mu\left(\frac{d}{2}\right)^3 \Delta d \frac{d\phi'}{dx}. \quad \text{(C.1)}$$

When the tube is in the form of a large split ring of radius a, and bending strains are assumed small, the displacement of the two ends under a perpendicular force F is given by

$$\Delta z = \int_0^{2\pi} d\phi \frac{dx}{d\phi}\frac{d\phi'}{dx}\frac{dz}{d\phi'}. \quad \text{(C.2)}$$

$(d\phi'/dx) = (4/\pi\mu d^3 \Delta d)\tau$, where $\tau = 2Fa$, $(dx/d\phi) = (a/\cos\theta)$, $(dz/d\phi')$ is the movement of the end of the ring caused by a strain $d\phi'$ at ϕ; $(dz/d\phi') = 2a\sin^2\phi/2$.

Therefore,

$$\Delta z = \int_0^{2\pi} \sin^2\frac{\phi}{2} d\phi \times \frac{16a^3F}{\pi\mu d^3 \Delta d\cos\theta} = \frac{16a^3F}{d^3\Delta d\mu\cos\theta}. \quad \text{(C.3)}$$

This is the distortion per coil in the helix. With $(\cot\theta/2\pi a)$ coils per centimeter, we find

$$K = \frac{\pi\mu d^3 \Delta d\sin\theta}{8a^2} \qquad \left(F = K\frac{\Delta z}{z}\right). \quad \text{(C.4)}$$

C.2. *Gravitational Sag.* The sag of the helix may be estimated by considering a cylindrical beam of radius a, whose compressional modulus is K. The effective Young's Modulus for this material is $K/\int dA$, where the integral is over the assumed cross section of the beam. The bending may be computed from[32]

$$\frac{d^2\delta(z)}{dz^2} = \frac{\mathcal{M}(z)}{\mathscr{Y}\int r^2\sin^2\phi\, dA} = \frac{\mathcal{M}(z)}{K}\frac{\int dA}{\int r^2\sin^2\phi\, dA} \equiv \frac{\mathcal{M}(z)}{K}\frac{\eta}{a^2}, \quad \text{(C.5)}$$

which serves to define the number η. For a thin-walled pipe of radius a, we find $\eta = 2$, and for a solid bar $\eta = 4$.

Assuming a distributed load w due to the weight of the helix, and point supports at intervals $\mathscr{L}$ on an infinitely long helix, the moment distribution is

$$\mathcal{M}(z) = \frac{\mathscr{L}wz}{2} - \frac{wz^2}{2} - \frac{w\mathscr{L}^2}{12}. \quad \text{(C.6)}$$

The deflection, by integrating Eq. (C.5) is

$$\delta(z) = \frac{\eta}{Ka^2}\left(\frac{\mathscr{L}wz^3}{12} - \frac{wz^4}{24} - \frac{w\mathscr{L}^2z^2}{24}\right). \quad \text{(C.7)}$$

Using the distributed loading, $w = \rho g(\pi d\Delta d/\sin\theta)$ g/cm, the maximum deflection is

$$\delta\left(\frac{\mathscr{L}}{2}\right) = -\frac{\rho g\mathscr{L}^4}{\mu d^2\sin^2\theta}\left(\frac{\eta}{48}\right). \quad \text{(C.8)}$$

C.3. *Electromagnetic Distortion.* Using the coordinate system of Fig. B.1, the stresses acting perpendicular to the surface of the helix wire are the magnetic stress

$$\sigma_M = \frac{1}{4\pi}B_\parallel^2 = \frac{\sin^2\omega t}{4\pi} \cdot \Big\{\Big[L^2\cos^2\phi' B_+^2 + (M + N\cos 2\phi')^2 B_-^2 + 2B_+B_-L(M + N\cos 2\phi')\cos\phi'\Big] \cdot \cos^2 b_0 z + X^2\sin^2\phi' B_r^2\sin^2 b_0 z - X\sin\phi' B_r[L\cos\phi' B_+ - (M + N\cos 2\phi')B_-] \cdot \sin b_0 z\cos b_0 z\Big\}, \quad \text{(C.9)}$$

and the electric stress

$$\sigma_E = \frac{1}{4\pi}E_\perp^2 = \text{Eq. (C.9)} \quad \text{(C.10)}$$

with the substitutions $\sin b_0 z \to \cos b_0 z$, $\cos b_0 z \to \sin b_0 z$, $\cos\omega t \to \sin\omega t$, $E_+ \to B_+$, $E_- \to B_-$, and $-E_z \to B_r$.

Since the largest distortions will be due to longitudinal forces, the axial force component is

$$\frac{dF_z}{d(a\phi)} = \int_0^{2\pi} d\phi'\sigma(\phi')\sin\phi' \text{ (dyn/cm of wire)}.$$

All of the trigonometric integrals vanish except for

$$\int_0^{2\pi} d\phi' \sin^2\phi' \cos 2\phi' = -\frac{\pi}{2} \text{ and } \int_0^{2\pi} d\phi' \sin^2\phi' = \pi;$$

thus,

$$\frac{dF_z}{d(a\phi)} = \frac{d}{16} \sin b_0 z \cos b_0 z X(2M - N) \cdot [B_r B_- \sin^2 \omega t + E_z E_- \cos^2 \omega t].$$

Averaging over t, and dividing by $\sin\theta$, we find the force acting per centimeter of waveguide

$$\frac{dF_z}{dz} = \frac{dX(M - N/2)}{128 \sin\theta} \cdot \sin 2b_0 z (B_r B_- + E_z E_-) \quad \text{(dyn/cm)} \qquad \text{(C.11)}$$

or,

$$\frac{dF_z}{dz} \cong \frac{0.06a}{\cos\theta} \sin\frac{4\pi z}{\lambda} (B_r B_- + E_z E_-) \quad \text{dyn/cm},$$

a result nearly independent of d/p, and close to the value gotten directly from the sheath model.

This force density produces a periodic force in the helix

$$F_z(z) = \int_0^z \frac{dF_z(z')\,dz'}{dz'} = \frac{0.06a}{\cos\theta} \frac{\lambda}{4\pi} (B_r B_- + E_z E_-) \cos\frac{4\pi z}{\lambda},$$

which produces a displacement

$$\Delta z = \frac{1}{K} \int_0^z dz' \int_0^{z'} dz'' \frac{dF_z(z'')}{dz''} = -\frac{0.06a}{K\cos\theta} \frac{\lambda^2}{16\pi^2} (B_r B_- + E_z E_-) \sin\frac{4\pi z}{\lambda}.$$

The pitch change is given by

$$\frac{\Delta p(z)}{p} \cong \frac{0.06a}{K\cos\theta} \frac{\lambda}{4\pi} (B_r B_- + E_z E_-) \cos\frac{4\pi z}{\lambda} = \frac{d}{dz}(\Delta z). \qquad \text{(C.12)}$$

The waveguide with a pitch $p = p_0 + \Delta p \cos(4\pi z/\lambda)$ has an average velocity which is different from the velocity in a waveguide with constant pitch p_0. Since $v = (Cp/2\pi a\gamma) f(g_0 c)$ (see Fig. 2), for non relativistic velocities,

$$\frac{dv}{dp} = \frac{v_0/p}{1 + g_0 c f'/f}. \qquad \text{(C.13}$$

The velocity on the helix is then

$$v \cong v_0 \left(1 + \frac{\Delta p/p}{1 + g_0 c f'/f} \cos\frac{4\pi z}{\lambda}\right), \quad \text{for } \Delta p/p \ll 1. \qquad \text{(C.14)}$$

f' is the slope of the curve in Fig. 2.

A velocity of the form $v(z) = v_0 + \Delta v \cos(4\pi z/\lambda)$ leads to an average velocity

$$v_{av} \cong v_0 \left[1 - 0.5 \left(\frac{\Delta v}{v_0}\right)^2\right]. \qquad \text{(C.15)}$$

This equation results from numerically integrating $x = \int v(x)\,dt$.

Thus, in a standing wave cavity, there is a frequency shift $\Delta\nu/\nu = (v_{av} - v_0)/v_0$.

For the helix example under Eq. (7), with an energy gain of (3 MeV/m), and neglecting f'/f, the frequency shift is $\Delta\nu/\nu \cong 2 \times 10^{-5}$.

APPENDIX D

The Double Helix Waveguide

Solving the sheath model of the double helix is just an extension of the methods of Sec. 3[19] to a more complicated geometry.

There is a helical sheath at $r = a$, with pitch angle θ_a, one at $r = b$ with θ_b, and a perfect conducting cylinder at $r = c$. In each of the three regions, the B_z and E_z fields are given by superpositions of $I_0(g_0 r)$ and $K_0(g_0 r)$. The other field components may be calculated from

$$B_r(r) = \frac{ib_0}{g_0^2} \frac{\partial B_z(r)}{\partial r} \qquad B_\phi(r) = \frac{ik}{g_0^2} \frac{\partial E_z(r)}{\partial r}$$

$$E_r(r) = \frac{ib_0}{g_0^2} \frac{\partial E_z(r)}{\partial r} \qquad E_\phi(r) = \frac{-ik}{g_0^2} \frac{\partial B_r(r)}{\partial r} \qquad \text{(D.1)}$$

All fields have the suppressed wave dependence $\exp(i[\omega t - b_0 z])$.

Labeling region I for $r < a$, II for $a < r < b$, and III for $b < r < c$, the following boundary conditions apply:

$$E_z^{\mathrm{I}}(a) = E_z^{\mathrm{II}}(a), \quad E_z^{\mathrm{II}}(b) = E_z^{\mathrm{III}}(b), \quad E_z^{\mathrm{III}}(c) = 0,$$
$$E_\phi^{\mathrm{I}}(a) = E_\phi^{\mathrm{II}}(a), \quad E_\phi^{\mathrm{II}}(b) = E_\phi^{\mathrm{III}}(b), \quad B_r^{\mathrm{III}}(c) = 0,$$
$$E_z^{\mathrm{I}}(a) \sin\theta_a + E_\phi^{\mathrm{I}}(a) \cos\theta_a = 0 = E_z^{\mathrm{III}}(b) \sin\theta_b + E_\phi^{\mathrm{III}} \cos\theta_b, \qquad \text{(D.2)}$$
$$B_z^{\mathrm{I}}(a) \tan\theta_a + B_\phi^{\mathrm{I}}(a) = B_z^{\mathrm{II}}(a) \tan\theta_a + B_\phi^{\mathrm{II}}(a), \text{ and}$$
$$B_z^{\mathrm{II}}(b) \tan\theta_b + B_\phi^{\mathrm{II}}(b) = B_z^{\mathrm{III}}(b) \tan\theta_b + B_\phi^{\mathrm{III}}(b).$$

There are eight unknown amplitudes:

$$E_z^{\mathrm{I}} = E_0 I_0(g_0 r), \qquad B_z^{\mathrm{I}} = B_0 I_0(g_0 r),$$
$$E_z^{\mathrm{II}} = E_1 I_0(g_0 r) + F_1 K_0(g_0 r),$$
$$B_z^{\mathrm{II}} = B_1 I_0(g_0 r) + C_1 K_0(g_0 r), \qquad \text{(D.3)}$$
$$E_z^{\mathrm{III}} = E_2 R(g_0 r), \quad \text{and} \quad B_z^{\mathrm{III}} = B_2 S(g_0 r),$$

[R and S are defined in Appendix A, and include $E_z(c) = 0$ and $B_r(c) = 0$] with the eight boundary condition equations.

As with the single helix, the solution of the eight simultaneous equations gives seven field amplitude ratios in terms of E_0, and a dispersion equation which is a quartic equation for $k/g_0 t_a$. In matrix form, the boundary equations are

$$\begin{bmatrix} I_{0a} & -I_{0a} & -K_{0a} & 0 & 0 & 0 & 0 & 0 \\ 0 & 0 & 0 & 0 & I_{1a} & -I_{1a} & K_{1a} & 0 \\ 0 & 0 & 0 & 0 & 0 & I_{1b} & -K_{1b} & U_b \\ 0 & I_{0b} & K_{0b} & -R_b & 0 & 0 & 0 & 0 \\ I_{0a} & 0 & 0 & 0 & -xI_{1a} & 0 & 0 & 0 \\ 0 & 0 & 0 & R_b & 0 & 0 & 0 & -x\frac{t_a}{t_b}U_b \\ xI_{1a} & -xI_{1a} & xK_{1a} & 0 & I_{0a} & -I_{0a} & -K_{0a} & 0 \\ 0 & \frac{t_a}{t_b}xI_{1b} & -\frac{t_a}{t_b}xK_{1b} & -\frac{t_a}{t_b}xT_b & 0 & I_{0b} & K_{0b} & -S_b \end{bmatrix} \times \begin{bmatrix} E_0 \\ E_1 \\ F_1 \\ E_2 \\ B_0 \\ B_1 \\ C_1 \\ B_2 \end{bmatrix} = 0, \qquad \text{(D.4)}$$

where the symbols I_{0a}, K_{0b}, etc. represent $I_0(g_0 a)$, $K_0(g_0 b)$, etc. and $x \equiv ik/g_0 t_a$.

The analytic expression found for $k/g_0 t_a$ by solving the determinant of the coefficients in Eq. (D.4) is very complicated and unenlightening. Because of this, the method of solution was to use a computer program to vary $k/g_0 t_a$ until the determinant was zero, and then to invert the seven by seven upper right-hand corner matrix to find the other amplitudes in terms of E_0.

Because of the large number (four) of independent parameters, it is not possible to present exhaustive results here. Figures 16–19 show how the dispersion equation and field amplitudes vary with the different parameters.

All of the results except for the frequency shift, of Appendices B and C, may be applied directly to the double helix. By calculating the dependence of the phase velocity on $\tan\theta_a$ and $\tan\theta_b$, it is also possible to estimate frequency shifts.

These results have been tested on an experimental double helix cavity. A one meter aluminum tube, 20-cm i.d., with two opposite parity helices was built. The helices were wound of $\frac{3}{8}$ in. copper tubing, and held in place with nylon threads. The radius of the inside helix to the center of the tubing was 5.6 cm, with a pitch of 1.3 cm. The outside helix had $b = 8.3$ cm, and $p_b = 2.6$ cm. Both helices were shorted to the outer tube at the ends. The propagation velocity was calculated by measuring the frequencies of the $n\lambda/2$ standing wave modes.

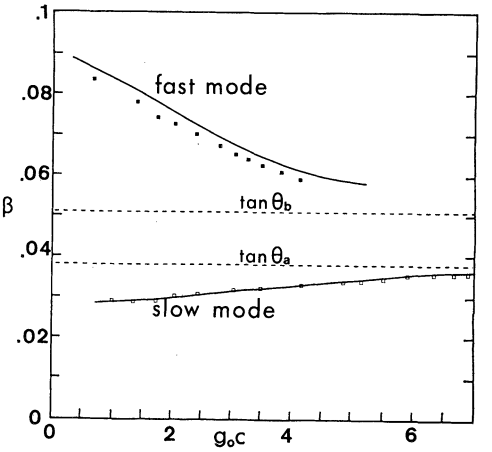

FIG. D.1. Dispersion curve for double helix cavity described in Appendix D. Solid lines are predictions of the sheath model, squares are measured values. Dashed lines show $\beta = \tan\theta$.

The modes were positively identified by a movable shorting wire.

The β vs $g_0 c$ curve was calculated with the sheath model using the exact radii and pitches mentioned above. The theoretical results are plotted in Fig. D.1 as a solid line, along with the experimental points. The dashed lines are the velocities which waves propagating along either helix would exhibit. The agreement is within 5 per cent for both modes, and the slopes of the curves are predicted exactly.

REFERENCES

1. W. Walkinshaw and K. Wyllie, Math. Memo. 57 (1948) (unpublished report).
2. K. Johnsen and H. Dahl, Chr. Michelsens Inst. Beretr. 14 (1951) (unpublished report).
3. K. Johnsen, Report CERN-PS/KJ 27 (1954) (unpublished report).
4. R. Servranckx, *Bull. Acad. Roy. Belg. Sci.*, **40,** 167 (1954); *ibid.*, **41,** 474 (1955).
5. L. W. Alvarez, H. Bradner, J. V. Franck, H. Gordon, J. D. Gow, L. C. Marshall, F. Oppenheimer, W. K. H. Panofsky, C. Richman, and J. R. Woodyard, *Rev. Sci. Instr.*, **26,** 111 (1955).
6. A. Septier, *C. R. Acad. Sci.* (Paris), **239,** 1367, 1476 (1954).
7. A. Septier, *L'Onde Elect.*, **36,** 966 (1956).
8. R. Servranckx and G. Dôme, *L'Onde Elect.*, **37,** 880 (1956).
9. A. K. Berezin, P. M. Zeidlits, A. M. Nekrashevich, and G. A. Silenok, *Sov. Phys. Tech. Phys.*, **4,** 730, 861 (1960).
10. D. P. R. Petrie, R. Bailey, D. G. Keith-Walker, H. Longley, and D. R. Chick, *Instn. Elec. Engr. Monograph* 441M (April 1961).
11. W. Muller and J. Rembser, *Nucl. Instr. Meth.*, **4,** 202 (1959).
12. H. Klein, P. Junior, J. Klabunde, O. Siart, H. Deitinghoff, P. Finke, and A. Schempp, *Proceedings of the International Conference on Nuclear Reactions Induced by Heavy Ions* (American Elsevier Publishing Co., New York, 1970) p. 491.
13. H. A. Schwettman, J. P. Turneaure, W. M. Fairbank, T. I. Smith, M. S. McAshan, P. B. Wilson, and E. E. Chambers, *IEEE Trans. Nucl. Sci.*, **NS-14,** No. 3, 336 (1967).
14. J. P. Turneaure and N. T. Viet, HEPL Report 612, Stanford University (October 1969) (unpublished report).
15. H. A. Schwettman, HEPL Report 578, Stanford University (August 1968) (unpublished report).
16. E. A. Lynton, *Superconductivity*, 3rd ed. (Methuen, London, 1969).
17. P. Flécher, J. Halbritter, R. Hietschold, P. Kneisel, W. Kühn, and O. Soltz, *IEEE Trans. Nucl. Sci.*, **NS-16,** No. 3, 1018 (1969).
18. J. R. Pierce, *Traveling Wave Tubes* (Van Nostrand, New York, 1950).
19. J. H. Bryant, *Elect. Comm.*, **31,** 50 (1954).
20. S. Sensiper, *Proc. I.R.E.*, **43,** 149 (1955).
21. L. Stark, *J. Appl. Phys.*, **25,** 1155 (1954).
22. J. D. Jackson, *Classical Electrodynamics* (John Wiley and Sons, New York, 1962).
23. A. J. Lichtenberg, *Phase Space Dynamics of Particles* (John Wiley and Sons, New York, 1969).
24. E. M. McMillan, *Phys. Rev.*, **80,** 493 (1950).
25. M. L. Good, *Phys. Rev.*, **92,** 538 (1953).
26. L. B. Mullett, AERE GP/M 147 (1953) (unpublished report).
27. Ya. B. Fainberg, *Sov. Phys. Tech. Phys.*, **4,** 506 (1959).
28. G. Teissier, A. Chabert, B. Veyron, LYCEN/6528, Inst. de Phys. Nucl. Lyon (1966) (unpublished report).
29. M. N. Kronick, private communication.
30. H. A. Schwettman, private communication.
31. W. R. Smythe, *Static and Dynamic Electricity*, 3rd ed. (McGraw-Hill Book Co., New York, 1968).
32. R. P. Feynman, R. B. Leighton, and M. Sands, *Lectures in Introductory Physics*, Vol. II (Addison-Wesley Publishing Co., Reading, Mass., 1964).

Received 2 October 1970;
Revised copy received 30 November 1970